

Post-synthetic modification of covalent organic frameworks for CO₂ electroreduction

Received: 18 January 2023

Accepted: 16 June 2023

Published online: 26 June 2023

Check for updates

Minghao Liu^{1,2,8}, Shuai Yang^{1,3,8}, Xiubei Yang^{1,4}, Cheng-Xing Cui^{5,6}✉, Guojuan Liu^{1,4}, Xuewen Li^{1,4}, Jun He², George Zheng Chen⁷, Qing Xu^{1,4}✉ & Gaofeng Zeng^{1,4}✉

To achieve high-efficiency catalysts for CO₂ reduction reaction, various catalytic metal centres and linker molecules have been assembled into covalent organic frameworks. The amine-linkages enhance the binding ability of CO₂ molecules, and the ionic frameworks enable to improve the electronic conductivity and the charge transfer along the frameworks. However, directly synthesis of covalent organic frameworks with amine-linkages and ionic frameworks is hardly achieved due to the electrostatic repulsion and predicament for the strength of the linkage. Herein, we demonstrate covalent organic frameworks for CO₂ reduction reaction by modulating the linkers and linkages of the template covalent organic framework to build the correlation between the catalytic performance and the structures of covalent organic frameworks. Through the double modifications, the CO₂ binding ability and the electronic states are well tuned, resulting in controllable activity and selectivity for CO₂ reduction reaction. Notably, the dual-functional covalent organic framework achieves high selectivity with a maximum CO Faradaic efficiency of 97.32% and the turnover frequencies value of 9922.68 h⁻¹, which are higher than those of the base covalent organic framework and the single-modified covalent organic frameworks. Moreover, the theoretical calculations further reveal that the higher activity is attributed to the easier formation of immediate *CO from COOH*. This study provides insights into developing covalent organic frameworks for CO₂ reduction reaction.

Covalent organic frameworks (COFs) are fully designable porous polymers, being comprised of organic knots and covalently connected linkers^{1–4}. The diversity of their building units allows them to have a high degree of structural tenability in terms of skeletons, porosities and topologies, resulting in tailorable functions^{5–8}. The functional COFs have been utilized in molecular absorptions, light emitters, photo conduction/catalysis, proton/lithium-ion conduction, and lithium-ion or lithium-sulfur batteries^{9–16}. Notably, the stable frameworks, large surface areas, open porous channels, and predictable

catalytic sites of COFs also allow them to be used as electrocatalysts in the electrochemical reactions, such as oxygen reduction reaction, oxygen evolution reaction, hydrogen evolution reaction, CO₂ reduction reactions (CO₂RR), and H₂O₂ synthesis^{17–22}. Electrocatalytic CO₂RR, which can produce high-value products from the greenhouse gas, is a promising strategy for addressing the CO₂ crisis. Owing to the molecular designability, COFs are an ideal class of templates to construct catalysts for CO₂RR^{23–26}. The catalytic behavior of COFs for CO₂RR is dependent on the structure and properties^{27–30}. From the

A full list of affiliations appears at the end of the paper. ✉ e-mail: chengxingcui@hist.edu.cn; xuqing@sari.ac.cn; zenggf@sari.ac.cn

perspective of structure, the types of catalytic centers, electronic states of the linker molecules, and linkage diversities have been adopted to assemble different catalytic COFs^{31–34}. By changing the building units or linkages, the corresponding properties of COFs, such as the binding ability of CO₂ and the electron conductivity, can be adjusted^{35–37}. Thus, a COF structure containing both amine bonds and ionizing skeletons, which enhance the binding ability of CO₂ molecules and the framework conductivity, respectively, is desirable for highly efficient CO₂RR.

The bottom-up synthetic approach is the most common method to directly construct functional COFs^{38–42}. Challenged by the steric hindrance effect, the solubility difference and the microscopic reversibility, however, some functionalities cannot be introduced directly into COFs via the bottom-up syntheses^{43–47}. For the pre-designed COF that contains amine bonds and ionizing skeletons, the existing covalent connection methods (e.g., boroxine rings⁴⁸, imine bonds⁴⁹ and β -ketoenamine linkage⁵⁰) do not support to obtain C–N linkage through the bottom-up synthesis directly, and the electrostatic repulsion effects of ionic building units impede the direct formation of ionizing skeletons. Alternatively, the post-synthetic modification strategy provides a promising chance to construct functional skeletons, pores, and linkages at the molecular level with controllable catalytic properties^{51–56}. Several single-step post-modifications were proposed to endow the base COFs with special properties^{57–60}. Deng et al. constructed imine-COFs by a post-reduction method to improve gas diffusion on electrode⁶¹. Guo et al. used Viologens (C₅H₄NR)₂⁺⁺ to construct a cationic radical framework from the 2,2'-bipyridine-based COF, which showed high photothermal conversion efficiencies⁶². Thus, it is expectable to obtain the COF with reduced imine linkages and ionic skeletons if the single-step post-modification of reduction and ionization can be well integrated. However, the integrated multilevel post-modification is rarely reported, because that not only a robust base COF is required but also the interference of multistep should be well avoided. In the view of COF design, 4,4',4'',4'''-(1,4-phenylenebis(azanetriyl))tetrabenzaldehyde (PATA) unit contains ammonium groups which are potential to transfer to ionic skeleton, and 5,10,15,20-tetrakis(4-aminophenyl)porphinato-cobalt (TAPP(Co)) unit can achieve efficient charge transfer due to their conjugated macrocyclic structures. In addition, we previously proved that CoTAPP-PATA-COF, composed by PATA and TAPP(Co), possesses good crystallinity, high surface areas, and excellent chemical stability²⁸. Thus, CoTAPP-PATA-COF is expected as a template for constructing multilevel post-synthetic modification COFs for CO₂RR.

In this study, we demonstrate a multilevel post-synthetic modification strategy to construct catalytic COFs for CO₂RR. The N⁺-NH-COF (N⁺: ionic modification; NH: reduction modification), which was constructed from CoTAPP-PATA-COF by the multilevel post-synthetic modification, showed a maximum CO faradic efficiency of 97.32% at –0.8 V with a CO current density of –28.01 mA cm^{–2} and the TOF value of 9922.68 h^{–1} at –1.0 V vs. RHE. The excellent electrocatalytic properties can be attributed to the superior binding ability of CO₂ molecules from C–N bonds and high conductivity from ionization skeletons in these COFs. The results showed that reduction of C=N linkages into the C–N bond and ionization of the linkers significantly improve the selectivity and activity.

Results

Chemistry and structure of N⁺-NH-COF

The base COF (CoTAPP-PATA-COF) was synthesized from CoTAPP and PATA using the solvothermal method described in our previous study¹⁷. The C=N linkages of the COF were reduced by adding NaBH₄ in dimethylacetamide (DMAC) to yield NH-COF, and the PATA units were ionized through in situ ammonium groups via Menshutkin reactions to obtain the N⁺-COF (Fig. 1a)⁶³. The base COF was modified through

sequential double post-functionalization (reduction and ionization) to obtain the N⁺-NH-COF (Fig. 1b).

The successful functionalization on the linkage reduction and the skeleton ionization were elucidated by the Fourier transform infrared spectroscopy (FTIR). Compared with the base COF, the C=N linkages at 1622 cm^{–1} were retained, while a peak raised at 1470 cm^{–1}, being ascribed to –N⁺-(CH₃)₂[–], in the FTIR spectrum of ionized N⁺-COF (Supplementary Fig. 1)^{31,56}. This reveals that the skeleton ionization was solely realized by the Menshutkin reaction. After the reduction modification, in contrast, the FTIR spectra of NH-COF and the N⁺-NH-COF revealed that the C=N vibrations at 1622 cm^{–1} were totally replaced by the signals of C–N at 1157 cm^{–1} (Supplementary Fig. 1)⁶¹. This indicates that the C=N linkages were fully converted into C–N bonds. Apart from C–N vibrations, furthermore, the ionic –N⁺-(CH₃)₂[–] was also detected for the FTIR spectrum of N⁺-NH-COF. Moreover, the Co–N bonds at 660 cm^{–1} were observed in all four COFs, indicating that the post-modifications were harmless to the Co–N coordinations.

The functionalizations of COFs were further confirmed by using the solid ¹³C cross-polarization/magic-angle spinning solid-state nuclear magnetic resonance (CP/MAS ssNMR, Supplementary Fig. 2). The C=N signals (148 ppm) in CoTAPP-PATA-COF and N⁺-COF were completely replaced by the C–N signals at 51 ppm for the NH-COF and N⁺-NH-COF. In addition, N⁺-COF and N⁺-NH-COF exhibited a peak belonging to methyl groups at 60 ppm. These results indicate that the successful reduction of –C=N and the methylation with charge state changes. On the other hand, the FTIR and ¹³C NMR results also reveal that the Menshutkin reaction is selective for the methylation of C–N bonds rather than the co-existed C=N bonds⁶⁰.

The crystalline structures of CoTAPP-PATA-COF, N⁺-COF, NH-COF and N⁺-NH-COF were investigated by the powder X-ray diffraction (PXRD) measurements. The PXRD pattern of base CoTAPP-PATA-COF showed the peaks of (011), (022), (031) and (001) facets at 5.15, 11.02, 12.23 and 21.84 °, respectively (Fig. 2a). The Pawley refinements revealed that the theoretical structures were in accordance with the experimental results with R_{wp} and R_p of 3.04% and 2.98%, respectively (Supplementary Table 1). According to the self-consistent charge density functional tight binding (DFTB) method, the base COF adopted AA stacking model, which enables to provide the open channels for mass transport (Fig. 2a). For the NH-COF, the peaks from (011), (310) and (001) were also identified (Fig. 2b). The Pawley refinements revealed that the simulated results were in accordance with the experimental results. And NH-COF adopts an eclipsed stacking in a PM space group with refined cell parameters of *a* = 22.51 Å, *b* = 23.45 Å, *c* = 5.41 Å, $\alpha = \beta = \gamma = 90^\circ$, with the corresponding R_{wp} of 2.64% and R_p of 2.06% (Supplementary Table 2). The N⁺-COF also displayed a good crystallinity with intense peaks at 5.15° (011), 11.12° (022), and 21.97° (001) (Fig. 2c). Both of the ionized COFs adopted AA stacking models. Notably, the crystallinity of the N⁺-NH-COF was well maintained after the double post-modifications, offering the peaks of (011), (002), (202) and (001) at 5.15, 11.12, 12.32 and 22.17 °, respectively (Fig. 2d). The highly crystalline structures were further confirmed by the Pawley refinements, delivering the corresponding R_{wp} of 2.67% and 3.78%, R_p of 2.26% and 3.03% for N⁺-COF and N⁺-NH-COF, respectively (Supplementary Tables 3, 4). Furthermore, the Pawley-refined patterns of four COFs illustrated that the AB stacking simulated structures were different to the experimental results (Supplementary Figs. 3–6).

The porous structures of COFs are crucial for the mass transport and the accessibility of active sites during electrocatalysis. Thus, the porosity of these COFs was investigated through the nitrogen sorption isotherm measurements at 77 K. The CoTAPP-PATA-COF exhibited a microporous sorption behaviour with a Brunauer–Emmett–Teller (BET) surface area (S_{BET}) of 943.72 m² g^{–1} (Fig. 3a, black curve), delivering a pore volume of 0.75 cm³ g^{–1} and a pore size of 1.1 nm (Supplementary Fig. 7). After the post modifications, the S_{BET} changed to 410.69, 659.05, and 340.19 m² g^{–1} for N⁺-COF, NH-COF, and N⁺-NH-COF,

respectively. In addition, the corresponding pore volumes declined to 0.45, 0.58, and 0.46 $\text{cm}^3 \text{g}^{-1}$, while the pore sizes kept no change for N^+ -COF, NH-COF, and N^+ -NH-COF, respectively (Supplementary Fig. 7). Considering the critical roles of CO_2 adsorption on CO_2RR , we investigated the CO_2 sorption behaviours at 273 K. The CO_2 uptakes of the CoTAPP-PATA-COF, N^+ -COF, NH-COF, and N^+ -NH-COF were 46.43, 27.80, 39.23, and 22.50 $\text{cm}^3 \text{g}^{-1}$ at 1 bar, respectively (Fig. 3b). Benefiting from the abundant C–N bonds, the NH-COF showed a high CO_2 adsorption capacity although its surface area and pore volume were relatively decreased. The role of C–N bonds on CO_2 adsorption was further checked by the CO_2 -temperature programmed desorption (CO_2 -TPD). Specifically, NH-COF exhibited a higher CO_2 desorption signal than that of base CoTAPP-PATA-COF, indicating the enhanced CO_2 adsorption capacity on C–N bonds (Supplementary Fig. 8).

The morphologies of the COFs were studied via the field-emission scanning electron microscopy (FE-SEM) and transmission electron microscopy (TEM). The post-modified COFs exhibited similar morphologies to that of base COF without significant morphological changes, suggesting that the structure is well preserved (Supplementary Figs. 9–12). This was further confirmed by the TEM observations (Supplementary Figs. 13–16). The high-resolution TEM (HR-TEM) images showed the ordered straight channels with diameters of ~ 1.1 nm in the COFs, in accordance with the pore sizes determined by the N_2 absorptions (Supplementary Fig. 17). It indicates that the mass transfer paths and the crystallinity of post-modified COFs were well protected. Energy dispersive X-ray spectroscopy (EDX) mapping images revealed that all elements were uniformly distributed in the COFs (Supplementary Figs. 18–21). Furthermore, the thermal gravimetric analysis (TGA) measurements showed that the post-modified COFs kept the similar thermal stability to that of base COF, and no significant mass

loss was observed at the temperature < 480 $^\circ\text{C}$ in N_2 (Supplementary Fig. 22).

In addition, the hydrophobicity of these COFs was evaluated by the water contact angle (WCA) measurements (Supplementary Fig. 23). The measured WCAs of the CoTAPP-PATA-COF, N^+ -COF, NH-COF, and N^+ -NH-COF were 121.6 ± 3.2 $^\circ$, 127.1 ± 2.6 $^\circ$, 129.4 ± 3.1 $^\circ$, and 128.3 ± 2.7 $^\circ$, respectively, indicating that the effects of post modifications on the surface hydrophilicity are negligible. Moreover, the hydrophobic behaviour of N^+ -NH-COF was further verified by water uptake test. The N^+ -NH-COF exhibited a low water vapour uptake capacity of 188 $\text{cm}^3 \text{g}^{-1}$ at 298 K and a inflection point at high relative pressures ($P/P_0 = 0.5$), which are in good agreement with the hydrophobic behaviours (Supplementary Fig. 24)⁶⁴. For the electrocatalysis of CO_2RR , the hydrophobic nature of catalyst is crucial to protect the active sites through suppressing the competitive adsorption of water, leading to the improvements of selectivity and energy efficiency⁶⁵.

The chemical structures and electron states of the COFs were investigated via X-ray photoelectron spectroscopy (XPS). The XPS spectra showed peaks corresponding to C, N, O, and Co in the prepared COFs (Supplementary Fig. 25). The Co content was 4.0, 4.0, 3.7, and 3.7 wt.% in the CoTAPP-PATA-COF, N^+ -COF, NH-COF, and N^+ -NH-COF, respectively, which are close to the values obtained from the inductively coupled plasma (ICP) measurements (i.e., 3.6, 3.5, 3.3, and 3.1wt.%, respectively). Furthermore, the high-resolution Co 2p spectra of the four COFs exhibited Co–N coordination, which confirmed that the Co–N sites were well retained after the multilevel post-modifications (Fig. 4a). In detail, compared with CoTAPP-PATA-COF (781.38 eV) and NH-COF (781.36 eV), the Co 2p_{3/2} spectra of N^+ -COF (780.92 eV) and N^+ -NH-COF (780.90 eV) showed a negative shift of -0.45 eV, which is ascribed to the electron-withdrawing effect of

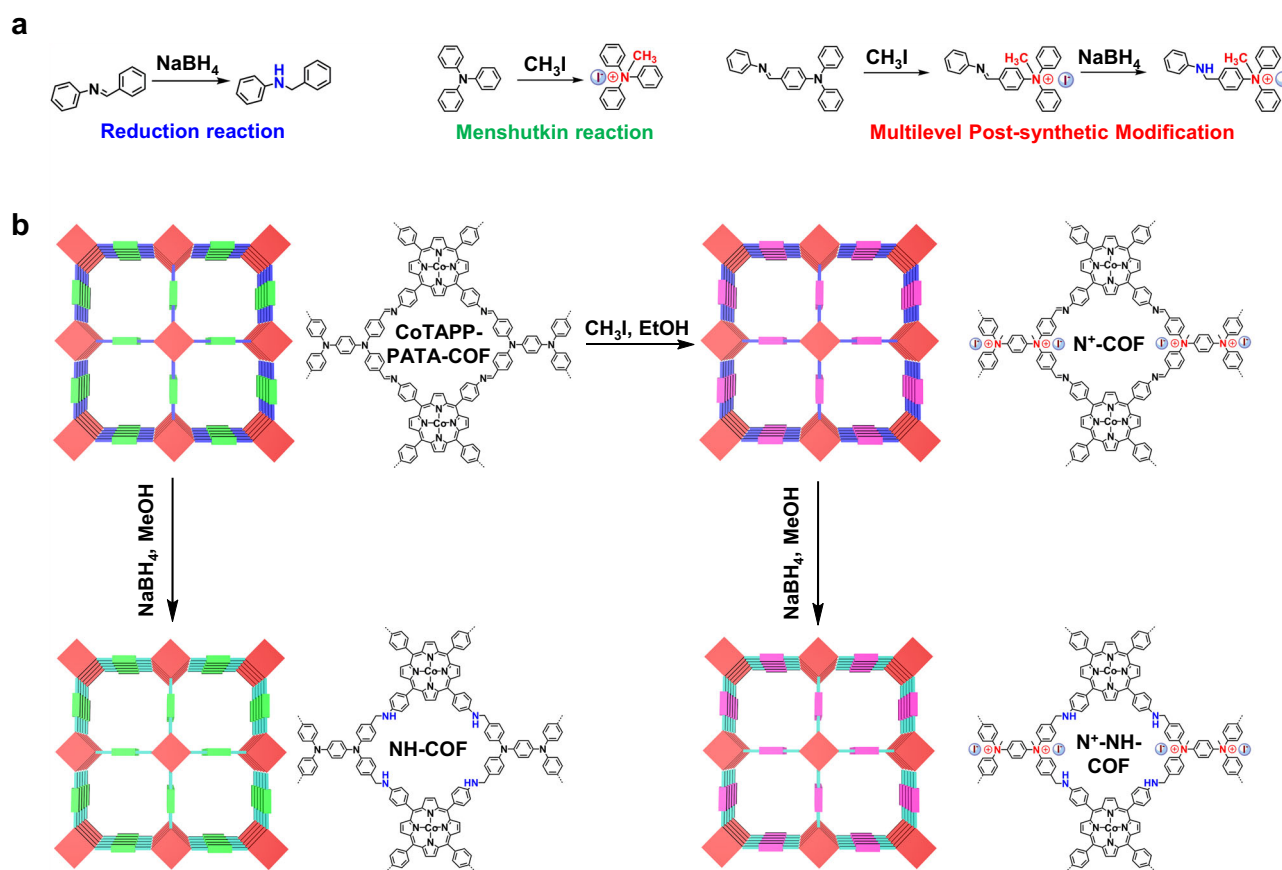


Fig. 1 | Schematic illustration of multilevel post-synthetic modification. **a** Effects of reduction reaction, Menshutkin reaction and multilevel post-synthetic modification on the bond change and charge state. **b** The synthesis of N^+ -COF, NH-COF and N^+ -NH-COF from the base COF (CoTAPP-PATA-COF).

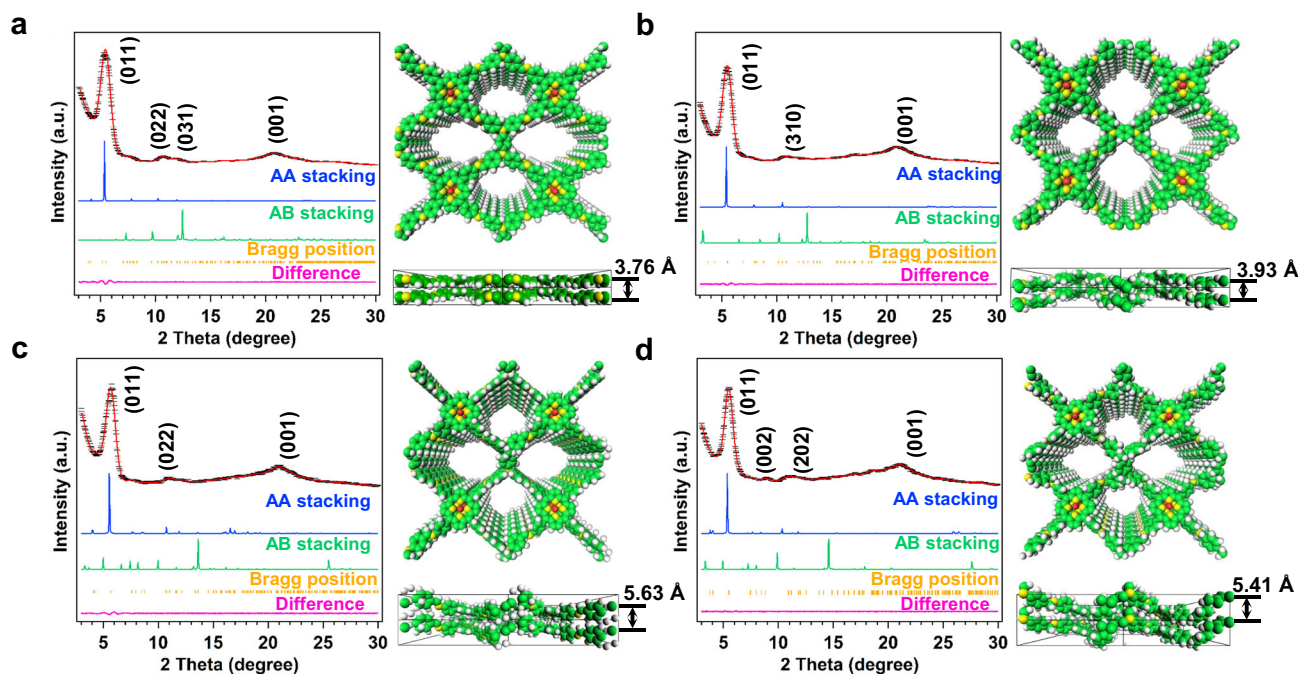


Fig. 2 | PXRD patterns of four COFs. The PXRD profiles and simulated structures of **a** CoTAPP-PATA-COF, **b** NH-COF, **c** N⁺-COF and **d** N⁺-NH-COF. Line colour follows: experimentally observed (black), Pawley refined (red), Bragg positions (orange)

and their difference (pink), simulated using the AA (blue) and staggered AB (green) stacking modes. Atom colour in the theoretically modelled eclipsed-AA stacking models: C-green, N-yellow, H-white, Co-red.

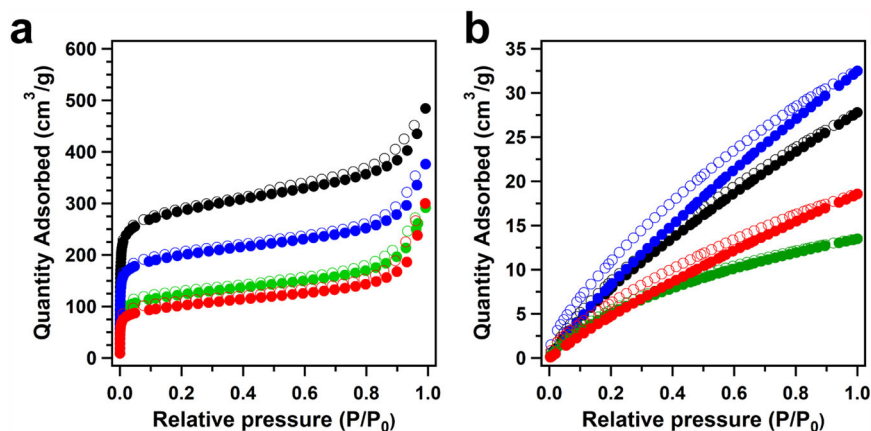


Fig. 3 | Gas adsorption characterization of four COFs. **a** The nitrogen-sorption isotherms at 77 K and **b** the CO₂ absorption curves at 273 K for CoTAPP-PATA-COF (black), N⁺-COF (green), NH-COF (blue) and N⁺-NH-COF (red).

methyl groups⁵⁶. This proves that the skeletons in N⁺-COF and N⁺-NH-COF have been ionized by the CH₃I modification. The high-resolution N 1s spectrum of the CoTAPP-PATA-COF was deconvoluted into three peaks of pyrrole N (398.29 eV), C=N (399.62 eV) and C-N (401.03 eV) with relative contents of 28.14, 55.88 and 15.97 at.%, respectively (Fig. 4b). In comparison, the N 1s spectrum of the NH-COF showed that the content of C=N was decreased to 14.74% while a C-NH peak appeared at 400.23 eV with a content of 46.09%. Moreover, the N⁺-COF displayed a peak at 402.34 eV, which was attributed to N⁺-CH₃ bonds⁶³. Due to the reduced linkages and the ionic linkers, the peaks of C-NH and N⁺-CH₃ were identified at 400.03 and 402.34 eV, respectively, in the N 1s spectrum of the N⁺-NH-COF (Fig. 4b). Therefore, the linkages and skeletons were fully modulated, as expected.

To investigate the different properties of the base and functionalized COFs, the ultraviolet–visible (UV-Vis) spectroscopy was adopted to determine their band gaps (Fig. 4c). Accordingly, the band gaps

of the CoTAPP-PATA-COF, N⁺-COF, NH-COF, and N⁺-NH-COF were determined as 2.68, 2.52, 2.66, and 2.67 eV, respectively (Fig. 4c, inset). As the conductivity increased with the decrease of gap value, the N⁺-COF has the highest conductivity compared with that of other COFs, indicating that the ionization units could improve the conductivity. To confirm the electronic conductivity change, the CoTAPP-PATA-COF, N⁺-COF, NH-COF and N⁺-NH-COF were measured by the four-probe method at 298 K (Supplementary Fig. 26). N⁺-NH-COF and N⁺-COF have similar electronic conductivities at $6.7 \times 10^{-9} \text{ S m}^{-1}$ and $8.1 \times 10^{-9} \text{ S m}^{-1}$, respectively, which are one order of magnitude larger than those of CoTAPP-PATA-COF ($8.5 \times 10^{-10} \text{ S m}^{-1}$) and NH-COF ($3.0 \times 10^{-10} \text{ S m}^{-1}$). It suggests that the ionized skeletons can promote the electron transfer along the frameworks, and thus improving the activity. The highest occupied molecular orbital (HOMO) and lowest unoccupied molecular orbital (LUMO) were calculated to investigate the electron conduction properties using the Mott–Schottky method (Supplementary Fig. 27).

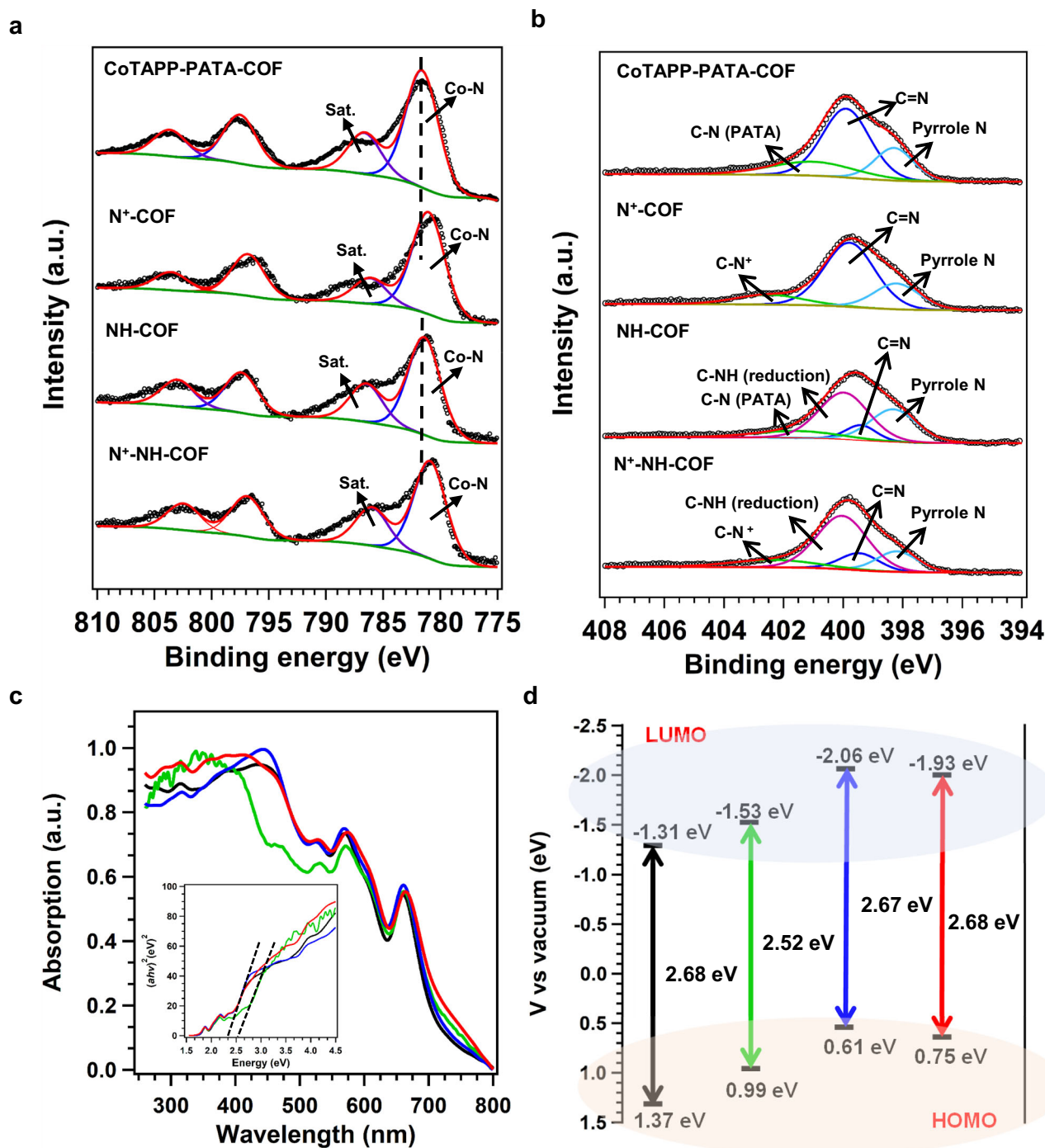


Fig. 4 | Electronic characterizations of four COFs. The XPS spectra of **a** Co 2*p* and **b** N 1*s* for CoTAPP-PATA-COF, N⁺-COF, NH-COF and N⁺-NH-COF. **c** The UV-vis absorption (insert: Tauc plots) and **d** the energy gap (HOMO and LUMO) for CoTAPP-PATA-COF (black), N⁺-COF (green), NH-COF (blue) and N⁺-NH-COF (red).

The HOMO positions of the CoTAPP-PATA-COF, N⁺-COF, NH-COF, and N⁺-NH-COF were 1.37, 0.99, 0.61, and 0.75 eV, respectively, suggesting that the multilevel post-synthetic modification effectively improved the reduction capacity of COFs (Fig. 4d)⁵⁸.

CO₂RR performance on N⁺-NH-COF

The CO₂RR performance of the catalytic COFs was investigated in a KHCO₃ aqueous solution (0.5M, pH 7.2) saturated with CO₂ using a standard two-compartment electrochemical cell. The COFs were mixed with carbon black at a weight ratio of 5/8. Firstly, the linear sweep voltammetry (LSV) measurements were conducted at a scan rate of 10 mV s⁻¹ from 0 to -1.0 V vs. RHE (Fig. 5a). Compared with N₂

saturated solution, a significantly higher current density was observed in the CO₂ saturated solution, indicating the superior CO₂ reduction activity of COFs (Supplementary Fig. 28). The LSV curves showed that the current densities of the CoTAPP-PATA-COF and NH-COF were close in the same potential range. In comparison, the current densities of N⁺-COF and N⁺-NH-COF were increased, suggesting that the ionized skeletons promoted electron transfer and enhanced the current density (Fig. 5a). The corresponding Tafel slope of the CoTAPP-PATA-COF was 236 mV dec⁻¹, which declined to 203, 197, and 184 mV dec⁻¹ for N⁺-COF, NH-COF, and N⁺-NH-COF, respectively (Fig. 5b). It suggests that the post modifications significantly improve the electrocatalytic CO₂RR kinetics³³.

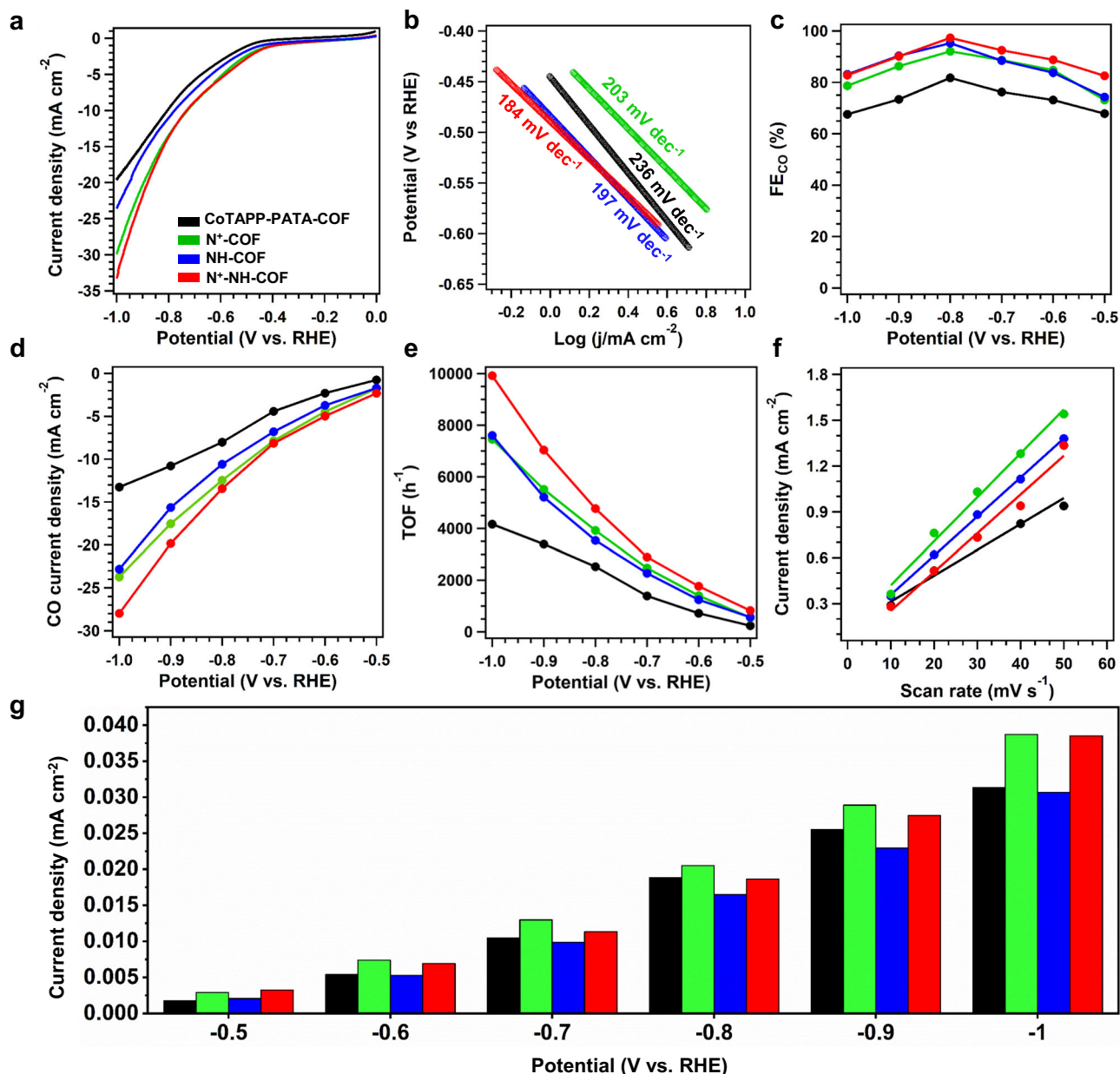


Fig. 5 | Electrochemical CO₂ reduction reaction on COFs. **a** LSV curves, **b** Tafel slopes, **c** CO faradaic efficiency, **d** the partial CO current density, **e** the corresponding TOF values, **f** the ECSA slopes and **g** the CO current density by the normalized ECSA for CoTAPP-PATA-COF (black), N⁺-COF (green), NH-COF (blue) and N⁺-NH-COF (red) from -0.5 to -1.0 V in 0.5 M KHCO₃ under CO₂ atmosphere.

The reduction products of CO₂RR were analysed via the gas and liquid chromatography, and only CO and H₂ were detected. The constant time-dependent total geometric current densities of the CoTAPP-PATA-COF, N⁺-COF, NH-COF, and N⁺-NH-COF were determined for each potential between -0.5 and -1.0 V for 1000 s, indicating that the COF catalysts had good stability (Supplementary Figs. 29–32). The CO Faradaic efficiencies (FE_{CO}) of the CoTAPP-PATA-COF were 67.84%, 73.11%, 76.26%, 81.75%, 73.42%, and 67.54% at -0.5, -0.6, -0.7, -0.8, -0.9, and -1.0 V, respectively (Fig. 5c, black curve). In addition to the selectivity, the activity was revealed by the partial CO current density (*j*_{CO}) of the catalyst. The CoTAPP-PATA-COF exhibited the highest *j*_{CO} of 13.26 mA cm⁻² at a potential of -1.0 V (Fig. 5c, black curve). The CO selectivity was remarkably improved on the COFs that contain C–N linkages and /or skeleton ionization. The N⁺-COF had considerably higher selectivity than the base COF at the same potential, delivering FE_{CO} of 73.12%, 84.75%, 88.71%, 92.07%, 86.31%, and 78.66% at -0.5,

-0.6, -0.7, -0.8, -0.9, and -1.0 V, respectively (Fig. 5c, green curve). The highest *j*_{CO} on N⁺-COF was 23.73 mA cm⁻² at -1.0 V, which was higher than that of the base COF (Fig. 5d, green curve). The FE_{CO} for the NH-COF were 74.26%, 83.75%, 88.49%, 95.26%, 90.31%, and 83.12%, which are higher than that of CoTAPP-PATA-COF and N⁺-COF at the same potentials (Fig. 5c, blue curve). The highest *j*_{CO} on NH-COF was 22.83 mA cm⁻² at -1.0 V, being also higher than that of base COF (Fig. 5d, blue curve). In comparison, the N⁺-NH-COF achieved FE_{CO} of 82.56%, 88.76%, 92.51%, 97.32%, 90.12%, and 82.78% from -0.5 to -1.0 V (Fig. 5c, red curve) and the highest *j*_{CO} of 28.01 mA cm⁻² at -1.0 V (Fig. 5d, red curve), which are higher than those of other COFs. Therefore, the C–N linkages improved the catalytic selectivity, and the ionic skeleton contributed to higher activity. The CO production turnover frequencies (TOFs) of the prepared COFs were obtained at different potentials by accounting the amount of CoTAPP units as electrocatalytically active sites. The highest TOF values obtained for

the CoTAPP-PATA-COF, N⁺-COF, NH-COF, and N⁺-NH-COF were 4166.19, 7453.19, 7604.63, and 9922.68 h⁻¹ at -1.0 V, respectively (Fig. 5e). As the N⁺-NH-COF yielded the highest TOF in compared to other COFs, it demonstrated that the multilevel post modification boosted both CO₂RR activity and CO selectivity of the base COF.

The electrochemical double layer capacitances (C_{dl}) were calculated using the cyclic voltammogram (CV) plots in a potential range of -0.16 to -0.36 V at the scan rates of 10–50 mV s⁻¹ (Supplementary Fig. 33). Correspondingly, the C_{dl} values for the CoTAPP-PATA-COF, N⁺-COF, NH-COF, and N⁺-NH-COF were 16.92, 26.34, 24.37, and 28.76 mF cm⁻², respectively (Fig. 5f)³⁸. To investigate the exposed active sites, the electrochemically active surface areas (ECSAs) of the COFs were then calculated by ECSA = C_{dl}/C_s, where the C_s is 0.04 mF cm⁻²⁶⁵. N⁺-NH-COF offered the highest ECSA (719) relative to CoTAPP-PATA-COF (423), N⁺-COF (659), and NH-COF (609), which is in line with its CO₂RR performance. Moreover, the ECSA of N⁺-COF was higher than the base COF and NH-COF, suggesting that the ionic frameworks provided more active sites⁶⁵. The normalized current densities on the COFs, i.e., j_{CO} per ECSA, were further evaluated (Fig. 5g). Within the potential range of -0.5 to -1.0 V, the ionized COFs of N⁺-COF and N⁺-NH-COF always exhibited the higher normalized current density than that of un-ionized COFs of CoTAPP-PATA-COF and NH-COF, confirming that the ionization helps to improve the COF activity towards CO₂RR. Furthermore, the Nyquist plots showed that the charge transfer resistances (R_{ct}) over N⁺-COF and N⁺-NH-COF were 36 and 24 Ω, respectively, being smaller than that of CoTAPP-PATA-COF (52 Ω) and NH-COF (42 Ω). This suggested that the ionization of skeletons enhanced the charge transfer capacity of COFs (Supplementary Fig. 34).

Moreover, the long-term stability of the N⁺-NH-COF was evaluated at -0.8 V in CO₂-saturated KHCO₃ for 25 h (Supplementary Fig. 35). The FE_{CO} kept stable around 97% and the relative current density (j/j₀) was >94.5% within 25 h, indicating the excellent long-term stability of N⁺-NH-COF for CO₂RR. To confirm the stability, the used N⁺-NH-COF was checked by the PXRD, FTIR and XPS measurements after the long-term stability test. The PXRD patterns showed that all peaks were fully retained, and peaks were well-retained after the long-term stability test (Supplementary Fig. 36). The FTIR spectra showed that all the peaks of the N⁺-NH-COF were well maintained (Supplementary Fig. 37). In addition, the Co 2p, I 3d and N 1s spectra showed the same states to that of fresh sample (Supplementary Figs. 38–40). Thus, the structure of the N⁺-NH-COF was retained.

Density functional theory calculations

To further understand the different performance of CoTAPP-PATA-COF, N⁺-COF, NH-COF and N⁺-NH-COF for CO₂RR, the density functional theory (DFT) calculations were carried out at the theoretical level of CAM-B3LYP/6-311 G(d) (SDD for Co) for the cluster models of these four COFs. Reasonable geometrical, electronical and thermodynamic information could be obtained with cluster models for COFs and similar systems^{66–68}. All structures along the potential energy surfaces were optimized without any restrictions. Frequencies were further performed to confirm that all optimized geometries are local minima and to obtain the Gibbs free energies. In the calculation, the four model molecules were labelled as M-CoTAPP-PATA-COF, M-I-N⁺-COF, M-NH-COF and M-I-N⁺-NH-COF, respectively, where the counter ion I⁻ was considered for the N⁺-COF and N⁺-NH-COF (Fig. 6a).

As shown in Fig. 6b and Supplementary Fig. 41, CO₂RR includes four steps: the absorption of CO₂, formation of *COOH and *CO where a proton coupled a single electron transfer take place for each step, and CO desorption from the active metal centre. From CO₂ to the product CO, the CO₂RR catalysed by M-I-N⁺-COF and M-I-N⁺-NH-COF are slightly endergonic, while those catalysed by M-CoTAPP-PATA-COF and M-NH-COF are exergonic. This is in accordance with the excellent catalytic ability of the four COFs. The relative free energies of *COOH

formation are higher than the initial state of CO₂ (i.e., the relative zero point of free energies), while the process from *COOH to the final product CO are largely exergonic. This indicates that the formation of *COOH is the rate control step. The lowest free energy changes of *COOH state for M-I-N⁺-NH-COF is in line with its best performance from a thermodynamic viewpoint. In addition, both M-I-N⁺-COF and M-I-N⁺-NH-COF have the lower free energy change values (ΔG) of *COOH than those of M-CoTAPP-PATA-COF and M-NH-COF, which indicates a stronger promotion effect of ionization than the neutral ones. As shown in Fig. 6c–e, we provided the main geometrical parameters and the Mulliken charges on main atoms for stationary points along the reaction pathway of M-I-N⁺-NH-COF catalysing CO₂RR. The oxygen O₁ atom in CO₂ coordinates with Co atom in M-I-N⁺-NH-COF. The Co-O1 bond is 2.734 Å and the charge transfer from M-I-N⁺-NH-COF to CO₂ is negligible because the total charge on CO₂ is nearly zero (Fig. 6c). The formation of *COOH by the proton transfer makes the distortion of CO₂ portion with the angle of O₁-C-O₂ decreases from 178.6° to 121.7°, along with the elongation of C-O₂ bond to from 1.154 Å to 1.343 Å (Fig. 6d). The shortened Co-C bond results a stronger charge transfer between M-I-N⁺-NH-COF and CO₂. The departure of *OH leads to the formation of *CO, where Co is of a vertical orientation with a Co-C-O bond angle of 168.1° (Fig. 6e). In addition, the main geometrical parameters and the Mulliken charges on main atoms for stationary points along the reaction pathway of CoTAPP-PATA-COF catalysing CO₂RR was shown in Supplementary Fig. 42. As the same as M-I-N⁺-NH-COF, CO₂ was adsorbed with the coordination between Co and oxygen, while the intermediates of *COOH and *CO were coordinated with Co with the C atoms in the case of CoTAPP-PATA-COF calculations.

Furthermore, in Fig. 6f–i, we listed the partitional density of states (PDOSs) of Co (blue lines), COOH (red lines) and remainder of *COOH (green lines) for adsorption state of COOH on M-CoTAPP-PATA-COF, M-I-N⁺-COF, M-NH-COF and M-I-N⁺-NH-COF. It could be found that the contribution of Co is larger in M-I-N⁺-COF and M-I-N⁺-NH-COF than in M-CoTAPP-PATA-COF and M-NH-COF, indicating that the introducing of methyl groups strengthens the electronic density on Co atom. This may promote the interaction between the Co and COOH portion during the reaction. All above calculated results are in consistent with the experimental observations.

Discussion

In this study, a multilevel post-function strategy was demonstrated to modulate the properties of COFs (porosity, crystallinity, and electron states), which can contribute to their tuneable catalytic performance for CO₂RR. By constructing catalytic COFs with ionic and NH linkers, the catalytic COFs allow catalysing CO₂RR with high activity and a maximum TOF value of 9922.68 h⁻¹ at -1.0 V, and high selectivity with the highest FE_{CO} of 97.32% at -0.8 V. This work provides us a more in-depth understanding of COFs and their applications in electrochemical energy storage and conversion systems. Meanwhile, it also guides us to construct multilevel post-synthetic modification COFs for achieving both tailored activity and high stability.

Methods

Synthesis of CoTAPP-PATA-COF

A mixture of 1-butanol / 1,2-dichlorobenzene (0.5 mL/0.5 mL), (PATA (14.2 mg, 0.03 mmol), TAPP(Co) (23.5 mg, 0.03 mmol), and an aqueous acetic acid solution (6 M, 0.1 mL) was degassed in a Pyrex tube (10 mL) by three freeze-pump-thaw cycles. The tube was sealed and heated at 120 °C for 3 days. The precipitate was collected by centrifugation, washed with tetrahydrofuran, and dried at 120 °C under vacuum overnight to give CoTAPP-PATA-COF in a yield of 87.6%.

Synthesis of NH-COF

A mixture of CoTAPP-PATA-COF (50 mg), NaBH₄ (100 mg), and methanol (50 mL) was stirred in a 100 mL flask for 12 h at 0 °C. The

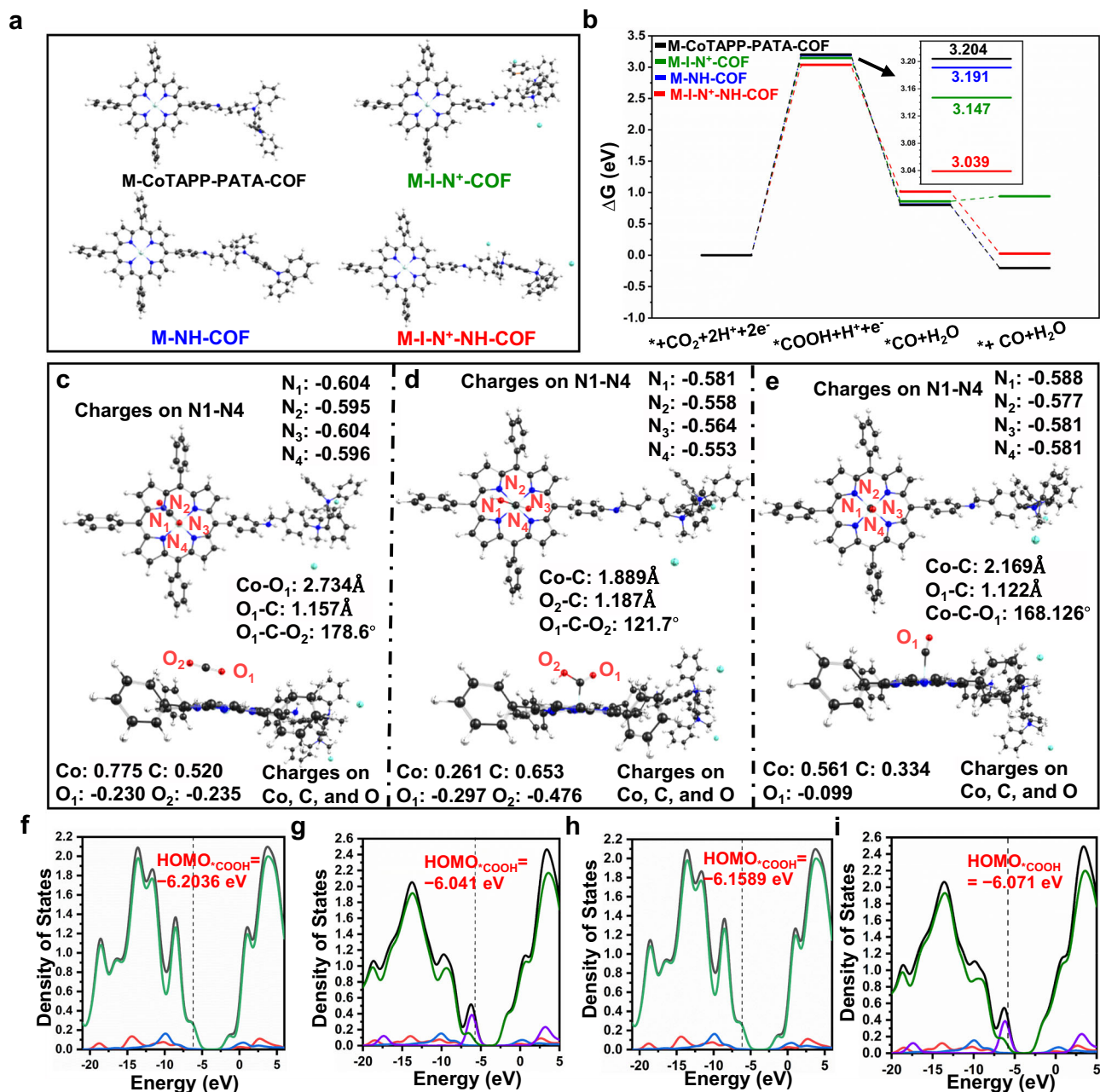


Fig. 6 | Theoretical calculation. **a** The optimized geometrical structures and **b** Calculated free energy change (ΔG) diagram of M-CoTAPP-PATA-COF, M-I-N⁺-COF, M-NH-COF and M-I-N⁺-NH-COF catalysing CO₂RR (M-Model). The optimized geometrical structures of stationary points along the reaction pathway of M-I-N⁺-NH-COF catalysing CO₂RR reaction, **c** CO₂^{*}, **d** COOH^{*}, **e** CO^{*}, along with the main geometrical parameters and the Mulliken charges on main atoms. The black, red,

white, blue, light cyan and dark cyan balls represent carbon, oxygen, hydrogen, nitrogen, cobalt and iodine atoms, respectively. The total density of states (TDOSs, black lines), partial density of states (PDOSs) of Co (blue lines), COOH (red lines), remainder of COOH^{*} (green lines) and counter ion I⁻ (purple line) for **f** M-CoTAPP-PATA-COF, **g** M-I-N⁺-COF, **h** M-NH-COF and **i** M-I-N⁺-NH-COF catalysing CO₂RR.

mixture was then poured into a large amount of ice water. After filtration, the white solid was washed three times with water and dried.

Synthesis of N⁺-COF

The cool stored 5 mL iodomethane (CH₃I) liquid was continuously added into a solution of the CoTAPP-PATA-COF (50 mg) in ethanol (200 mL) to be magnetically stirred at ambient temperature. Afterward, the mixture was vibrated at 60 °C for 24 h. The obtained white precipitate was collected and washed with ether followed by drying in vacuum for 6 h.

Synthesis of N⁺-NH-COF

A mixture of N⁺-COF (50 mg), NaBH₄ (100 mg, 2.64 mmol), and methanol (50 mL) was stirred in a 100 mL flask for 12 h at 0 °C. The mixture was then poured into a large amount of ice water. After filtration, the white solid was washed three times with water and dried.

Data availability

All data supporting the findings of this study are available within the article, as well as the Supplementary Information file. All other data supporting the findings of the study are available from the corresponding author upon request.

References

1. Zhao, X., Pachfule, P. & Thomas, A. Covalent organic frameworks (COFs) for electrochemical applications. *Chem. Soc. Rev.* **50**, 6871–6913 (2021).
2. Zhang, T., Zhang, G. & Chen, L. 2D conjugated covalent organic frameworks: defined synthesis and tailor-made functions. *Acc. Chem. Res.* **55**, 795–808 (2022).
3. Leith, G. A. et al. Confinement-guided photophysics in MOFs, COFs, and cages. *Chem. Soc. Rev.* **50**, 4382–4410 (2021).
4. Yang, D.-H., Tao, Y., Ding, X. & Han, B.-H. Porous organic polymers for electrocatalysis. *Chem. Soc. Rev.* **51**, 761–791 (2022).
5. Lyle, S. J., Waller, P. J. & Yaghi, O. M. Covalent organic frameworks: organic chemistry extended into two and three dimensions. *Trends Chem.* **1**, 172–184 (2019).
6. Liang, Z., Wang, H.-Y., Zheng, H., Zhang, W. & Cao, R. Porphyrin-based frameworks for oxygen electrocatalysis and catalytic reduction of carbon dioxide. *Chem. Soc. Rev.* **50**, 2540–2581 (2021).
7. Li, Y., Chen, W., Xing, G., Jiang, D. & Chen, L. New synthetic strategies toward covalent organic frameworks. *Chem. Soc. Rev.* **49**, 2852–2868 (2020).
8. Zhang, H., Gu, C., Yao, M.-S. & Kitagawa, S. Hybridization of emerging crystalline porous materials: synthesis dimensionality and electrochemical energy storage application. *Adv. Energy Mater.* **12**, 2100321 (2022).
9. Li, Z. et al. Three-dimensional covalent organic frameworks with hea topology. *Chem. Mater.* **33**, 9618–9623 (2021).
10. Wang, L. et al. A highly soluble, crystalline covalent organic framework compatible with device implementation. *Chem. Sci.* **10**, 1023–1028 (2019).
11. Yue, Y., Li, H., Chen, H. & Huang, N. Piperazine-linked covalent organic frameworks with high electrical conductivity. *J. Am. Chem. Soc.* **144**, 2873–2878 (2022).
12. Chen, X. et al. High-lithium-affinity chemically exfoliated 2D covalent organic frameworks. *Adv. Mater.* **31**, 1901640 (2019).
13. Kou, M. et al. Molecularly engineered covalent organic frameworks for hydrogen peroxide photosynthesis. *Angew. Chem. Int. Ed.* **61**, e202200413 (2022).
14. Liu, W. et al. Conjugated three-dimensional high-connected covalent organic frameworks for lithium–sulfur batteries. *J. Am. Chem. Soc.* **144**, 17209–17218 (2022).
15. Lei, Z. et al. Boosting lithium storage in covalent organic framework via activation of 14-electron redox chemistry. *Nat. Commun.* **9**, 576 (2018).
16. Wu, Z. et al. Engineering bismuth–tin interface in bimetallic aerogel with a 3D porous structure for highly selective electrocatalytic CO₂ reduction to HCOOH. *Angew. Chem. Int. Ed.* **60**, 12554–12559 (2021).
17. Liu, M. et al. Construction of catalytic covalent organic frameworks with redox-active sites for the oxygen reduction and the oxygen evolution reaction. *Angew. Chem. Int. Ed.* **134**, e202213522 (2022).
18. Guo, C. et al. Synergistic manipulation of hydrogen evolution and zinc ion flux in metal-covalent organic frameworks for dendrite-free Zn-based aqueous batteries. *Angew. Chem. Int. Ed.* **61**, e202210871 (2022).
19. Zhao, X. et al. Macro/microporous covalent organic frameworks for efficient electrocatalysis. *J. Am. Chem. Soc.* **141**, 6623–6630 (2019).
20. Liu, M. et al. Construction of atomic metal-N₂ sites by interlayers of covalent organic frameworks for electrochemical H₂O₂ synthesis. *Small* **18**, 2204757 (2022).
21. Karak, S. et al. A covalent organic framework for cooperative water oxidation. *J. Am. Chem. Soc.* **144**, 17661–17670 (2022).
22. He, C. et al. Metal-organic frameworks bonded with metal N-heterocyclic carbenes for efficient catalysis. *Natl. Sci. Rev.* **9**, nwab157 (2022).
23. Tang, J. et al. Large-area free-standing metalloporphyrin-based covalent organic framework films by liquid-air interfacial polymerization for oxygen electrocatalysis. *Angew. Chem. Int. Ed.* **135**, e202214449 (2023).
24. Lin, C. Y., Zhang, D., Zhao, Z. & Xia, Z. Covalent organic framework electrocatalysts for clean energy conversion. *Adv. Mater.* **30**, 1703646 (2018).
25. Wu, Q.-J. et al. Boosting electroreduction of CO₂ over cationic covalent organic frameworks: hydrogen bonding effects of halogen ions. *Angew. Chem. Int. Ed.* **62**, e202215687 (2022).
26. Han, B. et al. Two-dimensional covalent organic frameworks with cobalt(II)-phthalocyanine sites for efficient electrocatalytic carbon dioxide reduction. *J. Am. Chem. Soc.* **143**, 7104–7113 (2021).
27. Han, B. et al. Maximizing electroactive sites in a three-dimensional covalent organic framework for significantly improved carbon dioxide reduction electrocatalysis. *Angew. Chem. Int. Ed.* **61**, e202114244 (2022).
28. Zhu, H.-J. et al. Efficient electron transmission in covalent organic framework nanosheets for highly active electrocatalytic carbon dioxide reduction. *Nat. Commun.* **11**, 497 (2020).
29. Zhang, M.-D. et al. Conductive phthalocyanine-based covalent organic framework for highly efficient electroreduction of carbon dioxide. *Small* **16**, 2005254 (2020).
30. Wu, Q. et al. Construction of donor–acceptor heterojunctions in covalent organic framework for enhanced CO₂ electroreduction. *Small* **17**, 2004933 (2021).
31. An, S. et al. Constructing catalytic crown ether-based covalent organic frameworks for electroreduction of CO₂. *ACS Energy Lett.* **6**, 3496–3502 (2021).
32. Yan, X. et al. Superhydrophilic 2D covalent organic frameworks as broadband absorbers for efficient solar steam generation. *Angew. Chem. Int. Ed.* **61**, e202201900 (2022).
33. Zou, L. et al. Photoelectron transfer mediated by the interfacial electron effects for boosting visible-light-driven CO₂ reduction. *ACS Catal.* **12**, 3550–3557 (2022).
34. Wu, Q.-J., Liang, J., Huang, Y.-B. & Cao, R. Thermo-, electro-, and photocatalytic CO₂ conversion to value-added products over porous metal/covalent organic frameworks. *Acc. Chem. Res.* **55**, 2978–2997 (2022).
35. Chi, S.-Y. et al. Three-dimensional porphyrinic covalent organic frameworks for highly efficient electroreduction of carbon dioxide. *J. Mater. Chem. A* **10**, 4653–4659 (2022).
36. He, T. et al. Bottom-up interfacial design of covalent organic frameworks for highly efficient and selective electrocatalysis of CO₂. *Adv. Mater.* **34**, 2205186 (2022).
37. Zhou, T. et al. PEG-stabilized coaxial stacking of two-dimensional covalent organic frameworks for enhanced photocatalytic hydrogen evolution. *Nat. Commun.* **12**, 3934 (2021).
38. Huang, N. et al. A stable and conductive metallophthalocyanine framework for electrocatalytic carbon dioxide reduction in water. *Angew. Chem. Int. Ed.* **59**, 16587–16593 (2020).
39. Lu, M. et al. Rational design of crystalline covalent organic frameworks for efficient CO₂ photoreduction with H₂O. *Angew. Chem. Int. Ed.* **58**, 12392–12397 (2019).
40. Lu, C. et al. Atomic Ni anchored covalent triazine framework as high efficient electrocatalyst for carbon dioxide conversion. *Adv. Funct. Mater.* **29**, 1806884 (2019).
41. Liang, R.-R. et al. Rational design of crystalline two-dimensional frameworks with highly complicated topological structures. *Nat. Commun.* **10**, 4609 (2019).
42. Kibria, M. G. et al. Electrochemical CO₂ reduction into chemical feedstocks: from mechanistic electrocatalysis models to system design. *Adv. Mater.* **31**, 1807166 (2019).

43. Li, Y. et al. De novo design and facile synthesis of 2D covalent organic frameworks: a two-in-one strategy. *J. Am. Chem. Soc.* **141**, 13822–13828 (2019).
44. Su, Y. et al. Multi-component synthesis of a buta-1,3-diene-linked covalent organic framework. *J. Am. Chem. Soc.* **144**, 18218–18222 (2022).
45. Ning, G.-H. et al. Salicylideneanilines-based covalent organic frameworks as chemoselective molecular sieves. *J. Am. Chem. Soc.* **139**, 8897–8904 (2017).
46. Su, Y. et al. Crystalline and stable benzofuran-linked covalent organic frameworks from irreversible cascade reactions. *J. Am. Chem. Soc.* **142**, 13316–13321 (2020).
47. Wang, L. et al. Electrocleavage synthesis of solution-processed, imine-linked, and crystalline covalent organic framework thin films. *J. Am. Chem. Soc.* **144**, 8961–8968 (2022).
48. El-Kaderi, H. M. et al. Designed synthesis of 3D covalent organic frameworks. *Science* **316**, 268–272 (2007).
49. Uribe-Romo, F. J. et al. A crystalline imine-linked 3-D porous covalent organic framework. *J. Am. Chem. Soc.* **131**, 4570–4571 (2009).
50. Fang, Q. et al. 3D microporous base-functionalized covalent organic frameworks for size-selective catalysis. *Angew. Chem. Int. Ed.* **53**, 2878–2882 (2014).
51. Yang, Z. et al. Arylamine-linked 2D covalent organic frameworks for efficient pseudocapacitive energy storage. *Angew. Chem. Int. Ed.* **60**, 20754–20759 (2021).
52. Chen, W. et al. Modulating benzothiadiazole-based covalent organic frameworks via halogenation for enhanced photocatalytic water splitting. *Angew. Chem. Int. Ed.* **59**, 16902–16909 (2020).
53. He, C., Si, D.-H., Huang, Y.-B. & Cao, R. A CO₂-masked carbene functionalized covalent organic framework for highly efficient carbon dioxide conversion. *Angew. Chem. Int. Ed.* **134**, e202207478 (2023).
54. Wang, Y.-R. et al. Light, heat and electricity integrated energy conversion system: photothermal-assisted co-electrolysis of CO₂ and methanol. *Angew. Chem. Int. Ed.* **61**, e202212162 (2022).
55. Wang, S., Yang, L., Xu, K., Chen, H. & Huang, N. De novo fabrication of large-area and self-standing covalent organic framework films for efficient separation. *ACS Appl. Mater. Interfaces* **13**, 44806–44813 (2021).
56. Song, Y. et al. Atomically thin, ionic-covalent organic nanosheets for stable, high-performance carbon dioxide electroreduction. *Adv. Mater.* **34**, 2110496 (2022).
57. Jiang, S.-Y. et al. Amino-linked covalent organic frameworks through condensation of secondary amine with aldehyde. *J. Am. Chem. Soc.* **141**, 14981–14986 (2019).
58. Yue, Y. et al. Stable bimetallic polyphthalocyanine covalent organic frameworks as superior electrocatalysts. *J. Am. Chem. Soc.* **143**, 18052–18060 (2021).
59. Gong, L. et al. Covalent organic frameworks based on tetraphenyl-p-phenylenediamine and metalloporphyrin for electrochemical conversion of CO₂ to CO. *Inorg. Chem. Front.* **9**, 3217–3223 (2022).
60. Yang, B. & Zhang, C. Alkali-durable covalent organic frameworks carrying in situ ammonium as an ionic conductor toward hydroxide transport. *ACS Sustain. Chem. Eng.* **10**, 9749–9759 (2022).
61. Liu, H. et al. Covalent organic frameworks linked by amine bonding for concerted electrochemical reduction of CO₂. *Chem* **4**, 1696–1709 (2018).
62. Mi, Z. et al. Stable radical cation-containing covalent organic frameworks exhibiting remarkable structure-enhanced photothermal conversion. *J. Am. Chem. Soc.* **141**, 14433–14442 (2019).
63. Kalmutzki, M. J., Diercks, C. S. & Yaghi, O. M. Metal-organic frameworks for water harvesting from air. *Adv. Mater.* **30**, 1704304 (2018).
64. Zhang, X. et al. Insight into heterogeneous electrocatalyst design understanding for the reduction of carbon dioxide. *Adv. Energy Mater.* **12**, 2201461 (2022).
65. Li, N. et al. Boosting electrocatalytic CO₂ reduction with conjugated bimetallic Co/Zn polyphthalocyanine frameworks. *CCS Chem.* **5**, 1130–1143 (2022).
66. Mandal, M., Cramer, C. J., Truhlar, D. G., Sauer, J. & Gagliardi, L. Structure and reactivity of single-site vanadium catalysts supported on metal-organic frameworks. *ACS Catal.* **10**, 10051–10059 (2020).
67. Zhai, L. et al. CoN₅ sites constructed by anchoring Co porphyrins on vinylene-linked covalent organic frameworks for electroreduction of carbon dioxide. *Small* **18**, 2200736 (2022).
68. Lin, C. et al. Covalent organic frameworks with tailored functionalities for modulating surface potentials in triboelectric nanogenerators. *Angew. Chem. Int. Ed.* **61**, e202211601 (2022).

Acknowledgements

The authors acknowledge the financial support from the Natural Science Foundation of Shanghai (20ZR1464000 (Q.X.) and 22ZR1470100 (G.Z.)), the National Natural Science Foundation of China (21878322 (G.Z.), 22075309 (G.Z.)), the Youth Innovation Promotion Association of Chinese Academy of Sciences (Q.X.), and the Biomaterials and Regenerative Medicine Institute Cooperative Research Project (2022LHA09 (G.Z.)), Shanghai Jiaotong University School of Medicine. The Funding for Internationalization Training HighLevel Talent in Henan Province and Open Project of ZhengZhou JiShu Institute of AI Science (ZZJSA2023001 (C.-X.C.)).

Author contributions

Q.X. conceived the idea and designed the experiments. M.L. and S.Y. performed the experiments. C.-X.C. contributed to the theory calculation part. X.Y., G.L. and X.L. participated in some experiments. M.L., J.H., G.-Z.C., Q.X. and G.Z. wrote and revised the manuscript. All the authors contributed to the data interpretation, discussion, and manuscript revision. All authors have given approval to the final version of the manuscript. M.L. and S.Y. contributed equally to this work.

Competing interests

The authors declare no competing interests.

Additional information

Supplementary information The online version contains supplementary material available at <https://doi.org/10.1038/s41467-023-39544-9>.

Correspondence and requests for materials should be addressed to Cheng-Xing Cui, Qing Xu or Gaofeng Zeng.

Peer review information *Nature Communications* thanks Yuan-Biao Huang and the other, anonymous, reviewers for their contribution to the peer review of this work. A peer review file is available.

Reprints and permissions information is available at <http://www.nature.com/reprints>

Publisher's note Springer Nature remains neutral with regard to jurisdictional claims in published maps and institutional affiliations.

Open Access This article is licensed under a Creative Commons Attribution 4.0 International License, which permits use, sharing, adaptation, distribution and reproduction in any medium or format, as long as you give appropriate credit to the original author(s) and the source, provide a link to the Creative Commons license, and indicate if changes were made. The images or other third party material in this article are included in the article's Creative Commons license, unless indicated otherwise in a credit line to the material. If material is not included in the article's Creative Commons license and your intended use is not permitted by statutory regulation or exceeds the permitted use, you will need to obtain permission directly from the copyright holder. To view a copy of this license, visit <http://creativecommons.org/licenses/by/4.0/>.

© The Author(s) 2023

¹CAS Key Laboratory of Low-Carbon Conversion Science and Engineering, Shanghai Advanced Research Institute, Chinese Academy of Sciences, Shanghai 201210, P. R. China. ²Department of Chemical and Environmental Engineering, University of Nottingham Ningbo China, Ningbo 315199, P. R. China. ³School of Physical Science and Technology, ShanghaiTech University, Shanghai 201210, P. R. China. ⁴School of Chemical Engineering, University of Chinese Academy of Sciences, Beijing 100049, P. R. China. ⁵School of Chemistry and Chemical Engineering, Institute of Computational Chemistry, Henan Institute of Science and Technology, Xinxiang 453003, P. R. China. ⁶ZhengZhou JiShu Institute of AI Science, Zhengzhou 451162, P. R. China. ⁷Department of Chemical and Environmental Engineering, University of Nottingham, Nottingham NG7 2RD, UK. ⁸These authors contributed equally: Minghao Liu, Shuai Yang. ✉e-mail: chengxingcui@hist.edu.cn; xuqing@sari.ac.cn; zenggf@sari.ac.cn